A Phenomenological Framework and Exploratory Post-Merger Search for Gravitational-Wave Echoes from Quantum-Corrected Horizons

Tushar Sen *

Technology Department, University of Mumbai, India.

Abstract

Post-merger gravitational-wave observations provide a direct observational test of classical black-hole horizon structure in the strong-field regime. In this work, we develop a self-consistent semiclassical scattering framework and an off-source calibrated matched-filter pipeline to search for post-merger gravitational-wave echoes motivated by horizon-scale quantum coherence. Modeling overlapping interior singularity wavefunctions ($\Psi_{\rm sing}$) via the semiclassical Einstein field equations, we enforce covariant stress-energy conservation ($\nabla^\mu \langle \hat{T}_{\mu\nu} \rangle_\Psi = 0$) across the near-horizon boundary layer and solve the sourced Regge–Wheeler equation with a complex boundary impedance $Z^Q_{\ell m}(\omega)$. This yields a Fabry–Pérot echo transfer function $\mathcal{K}_{\ell m}(\omega)$ parameterized by the barrier transmission $T_{\rm barrier}$, effective horizon reflectivity $R_{\rm eff}$, and logarithmic round-trip delay $\Delta t_{\rm echo} \propto M_f \ln(M_f/m_P)$. Distinguishing the mesoscopic localization scale $\sigma = \sqrt{\ell_P R_s} = 1.720 \times 10^{-15}\,\mathrm{m}$ from a Planckian proper-distance cutoff $\ell_{\rm prop} = \ell_P$, we reconcile the characteristic round-trip delays for a GW150914-like remnant ($M_f = 62.0\,M_\odot$, $a_* = 0.67$) as $\Delta t^{(\sigma)}_{\rm echo} = 0.133\,\mathrm{s}$ and $\Delta t^{(\ell_P)}_{\rm echo} = 0.265\,\mathrm{s}$, respectively. Applying 248 s disjoint off-source Welch power spectral density estimation and 5σ dynamic glitch gating to open LIGO O1/O2 strain data, we suppress narrowband spectral artifacts in Livingston ($\rho_{\rm echo,L1} = 1.13$) and isolate the post-merger residual in Hanford ($\rho_{\rm echo,H1} = 0.50$, empirical $p_{\rm emp} = 0.0260$ across 1,000 background trials). While no statistically significant echo detection is observed in GW150914, 500-trial Monte Carlo software injections place a 95%-confidence observational upper bound of $R_{\rm eff} \lesssim 0.55$, disfavoring lossless maximally reflective horizons while remaining fully consistent with partially dissipative semiclassical models. Extending the pipeline across GW151226 ($20.8\,M_\odot$) and GW170104 ($48.7\,M_\odot$) confirms stable background suppression across the stellar-mass spectrum and establishes quantitative sensitivity benchmarks for third-generation terrestrial detectors and the space-based LISA mission.

Keywords: *Kerr spacetime, black hole singularity, quantum horizon interference, gravitational-wave echoes, Regge-Wheeler equation, GW150914*

1. Introduction

The historic detection of transient gravitational-wave signals from binary black hole coalescences by the Laser Interferometer Gravitational-Wave Observatory (LIGO) and the Virgo collaboration has initiated an unprecedented observational era in strong-field gravity Abbott et al. (2016). In classical general relativity, these ultra-compact objects are modeled via smooth, deterministic geometric frameworks that terminate inevitably at an infinitely dense central singularity Schwarzschild (1916). However, this smooth description inherently fails at the core boundaries where the local curvature invariants diverge. This breakdown creates the long-standing black hole information paradox, exposing a fundamental incompatibility between the continuous geometry of spacetime and the local conservation of quantum information Hawking (1976). To bypass these scale contradictions, modern quantum gravity models increasingly suggest that the event horizon may act as a physical, partially reflective, dissipative membrane or a sharp effective potential barrier capable of back-scattering trapped gravitational perturbations as discrete, decaying post-merger echoes Abedi et al. (2017), Cardoso et al. (2016).

*Editorial Board Member, *Astronomy & Astrophysics (CAUCASUS)*, Samtskhe-Javakheti State University, Georgia — Corresponding author: tushar.sen@gmail.com

doi: https://doi.org/10.52526/25792776-26.73.2-456

While traditional echo frameworks offer an intriguing macroscopic look at horizon-scale physics, they typically treat these boundaries as static, isolated phenomenological shells. These models often leave the deep interior dynamics and the ultimate fate of the infalling matter unaddressed. In this paper, we propose a novel paradigm that shifts the analytical focus to the intrinsic quantum mechanics of the central core. We postulate that because a physical singularity is compressed to subatomic scales during gravitational collapse, it can no longer be modeled as a classical localized point mass. Instead, the singularity must exist probabilistically anywhere within a confined central core sphere, governed strictly by an anisotropic quantum wave function ($\Psi_{\rm sing}$) satisfying a localized Wheeler-DeWitt framework Singh & Nandy (2024b). By treating the core singularity as a delocalized quantum mechanical state rather than a classical point, the unphysical mathematical infinities are resolved through standard wave function smearing.

When two binary black holes undergo a highly dynamical coalescence, their interior subatomic singularities do not experience a classical point-like collision. Rather, the merger event triggers a macroscopic quantum mechanical overlap and subsequent interference of their distinct, evolving singular wave functions. As these singular wave functions combine, resonate, and oscillate within the non-linear interior geometry, they act as highly coherent dynamical source terms. These fluctuating quantum distributions emit secondary metric perturbations that propagate outward from the core. Upon reaching the effective horizon barrier at a scale-free quantum localization boundary $\sigma = \sqrt{\ell_P R_s}$, these deep interior waves partially reflect and partially escape, manifesting as the macroscopically detectable gravitational-wave echoes targeted by our post-merger matched-filter pipeline (Oshita et al., 2020).

By testing this framework against open LIGO O1/O2 strain data for GW150914, GW151226, and GW170104 using IMRPhenomD baseline templates and off-source noise calibration, we place quantitative observational constraints on effective horizon reflectivity ($R_{\rm eff} \lesssim 0.55$ at 95% confidence) while establishing a falsifiable mapping between interior core states and post-merger ringdown observables. This approach provides a clear, falsifiable mapping that connects the microscopic quantum state of interior singularities directly to macroscopically verifiable features in the post-merger ringdown spectrum. Consequently, this framework provides a structural mechanism for horizon echoes that is directly driven by the core quantum states, offering a unique avenue to test the subatomic interior of black holes via precision gravitational-wave observations.

2. Literature Review and Theoretical Context

The search for signatures of quantum gravity in the strong-field regime has catalyzed a major paradigm shift in black hole perturbation theory. The foundational observation of gravitational waves from the binary black hole merger `GW150914` by the LIGO Scientific Collaboration and Virgo Collaboration Abbott et al. (2016) provided the first experimental proof of dynamic space-time curvatures. However, while standard numerical relativity models match the bulk inspiral flawlessly, the classical general relativistic framework demands that infalling matter terminates at an infinitely dense point singularity where smooth geometry collapses. To resolve the resulting horizon information paradox, Cardoso, Franzin, and Pani Cardoso et al. (2016) introduced a second foundational baseline. They demonstrated that if the event horizon is replaced by a hard, reflective Planck-scale boundary or firewall, the traditional quasinormal mode ringdown is modulated by trailing, repeating gravitational-wave echoes. This theoretical mechanism was first observationally tested by Abedi, Dykaar, and Afshordi Abedi et al. (2017), who presented controversial, tentative empirical evidence for echo packet clusters within public strain data.

Following these early benchmarks, phenomenological echo research branched heavily into near-horizon scattering mechanics. Researchers constructed complex, top-down membrane profiles, such as the frequency-dependent Boltzmann reflectivity frameworks explored by Oshita, Wang, and Afshordi Oshita et al. (2020), or the effective potential barrier mappings developed by Konoplya Konoplya (2022). Concurrently, Manikandan and Rajeev Manikandan & Rajeev (2022) proposed an Andreev-like reflection analogy where horizon-scale quantum fluctuations back-scatter metric perturbations, a theme expanded by Maggio et al. Maggio et al. (2022) to constrain alternative exotic compact objects. More recently, model-agnostic search algorithms deployed on transient strain catalogs by the LVK Collaboration have established stringent upper bounds on echo amplitudes, emphasizing the acute need for highly specialized, physically grounded template architectures rather than broad statistical searches.

Despite the mathematical sophistication of these scattering frameworks, a major gap persists in the existing literature: traditional models treat the reflective horizon as a passive, static, or isolated boundary

shell. The entire black hole interior is either excised or treated as a classical vacuum, ignoring the dynamical feedback of the collapsing core mass.

Our paper directly addresses this deficit, introducing a major theoretical contribution and a completely unique approach to the field. Our core novelty lies in the postulation that the horizon echo is not an isolated boundary reflection, but is an emergent manifestation of the subatomic quantum mechanics of the interior core. We build directly upon recent developments in canonical loop quantum gravity and Wheeler-DeWitt mathematical frameworks where classical point-like singularities are successfully resolved. As demonstrated by Singh and Nandy Singh & Nandy (2024b), the central Schwarzschild singularity can be replaced by a non-singular probability amplitude distribution with a finite wave function limit at $r \to 0$. This interior structure aligns with regular de Sitter core profiles evaluated by Capozziello et al. Capozziello et al. (2024), as well as dynamic collapse profiles modeled by Wang et al. Wang et al. (2020). Furthermore, the structural framework of a delocalized, regular core follows the non-point redefinitions outlined by Büyük Büyük (2026), where quantum back-reactions smear out the unphysical infinities.

By synthesizing these independent interior core frameworks with macroscopic data-driven phenomenology, our paper offers an entirely unique, first-principles derivation of the echo source term. Instead of assuming an arbitrary, ad-hoc reflectivity factor on a static exterior shell, we model the macroscopic overlap, interference, and oscillation of the distinct subatomic singularity wave functions ($\Psi_{\rm sing}$) during a binary merger. These colliding wavefunctions act as active, coherent source distributions that project space-time perturbations outward from the interior core sphere. When these core waves encounter the scale-free quantum localization boundary $\sigma = \sqrt{\ell_P R_s}$, they generate the highly phase-coherent echo patterns searched for by our post-merger matched-filter pipeline. This interior-to-exterior mapping provides the field with a robust, physically comprehensive framework, shifting horizon echoes from an isolated boundary assumption to a direct, verifiable probe of interior subatomic singularity wave functions.

3. Theoretical Framework: Semiclassical Horizon Boundary Conditions and Echo Generation

3.1. Interior Quantum Coherence and Effective Stress-Energy Conservation

To model post-merger departures from classical general relativity without invoking a specific ultraviolet completion, we treat the near-horizon quantum interior as a macroscopic coherent state described by an effective collective wavefunction $\Psi_{\rm sing}(r,t)$. In the semiclassical regime, the back-reaction of the interior quantum state onto the background spacetime metric $g_{\mu\nu}$ is governed by the semiclassical Einstein field equations:

$$G_{\mu\nu} = \frac{8\pi G}{c^4}\langle \hat{T}_{\mu\nu}\rangle_\Psi, \tag{1}$$

where $\langle \hat{T}_{\mu\nu}\rangle_\Psi$ denotes the renormalized expectation value of the stress-energy tensor associated with $\Psi_{\rm sing}$.

Because the Einstein tensor satisfies the contracted Bianchi identity $\nabla^\mu G_{\mu\nu} = 0$, consistency of Eq. (1) strictly requires covariant conservation of the effective stress-energy tensor across the near-horizon transition layer:

$$\nabla^\mu \langle \hat{T}_{\mu\nu}\rangle_\Psi = \frac{1}{\sqrt{-g}}\partial_\mu\left(\sqrt{-g}\langle \hat{T}^\mu{}_\nu\rangle_\Psi\right) - \frac{1}{2}(\partial_\nu g_{\alpha\beta})\langle \hat{T}^{\alpha\beta}\rangle_\Psi = 0. \tag{2}$$

For a spherically symmetric background line element of the form

$$ds^2 = -f(r)\,c^2dt^2 + f(r)^{-1}dr^2 + r^2(d\theta^2 + \sin^2\theta\, d\phi^2), \qquad f(r) = 1 - \frac{R_s}{r}, \tag{3}$$

where $R_s = 2GM/c^2$ is the Schwarzschild radius, evaluating the radial ($\nu = r$) component of Eq. (2) yields the hydrostatic equilibrium and radial flux balance relation:

$$\frac{d\langle \hat{T}^r{}_r\rangle_\Psi}{dr} + \frac{2}{r}\left(\langle \hat{T}^r{}_r\rangle_\Psi - \langle \hat{T}^\theta{}_\theta\rangle_\Psi\right) + \frac{f'(r)}{2f(r)}\left(\langle \hat{T}^r{}_r\rangle_\Psi - \langle \hat{T}^t{}_t\rangle_\Psi\right) = 0. \tag{4}$$

Across the thin quantum boundary surface located at $r = r_0 = R_s + \Delta r$, integrating Eq. (4) across the boundary thickness enforces continuity of the radial momentum flux and establishes the Israel–Darmois surface stress-energy junction condition:

$$\left[\langle \hat{T}^r{}_r\rangle_\Psi\right]_{r_0^-}^{r_0^+} = 0, \qquad S_{\mu\nu} = -\frac{c^4}{8\pi G}\left([K_{\mu\nu}] - h_{\mu\nu}[K]\right), \tag{5}$$

doi: https://doi.org/10.52526/25792776-26.73.2-456

where $K_{\mu\nu}$ is the extrinsic curvature of the timelike boundary hypersurface $r = r_0$ and $h_{\mu\nu}$ is its induced metric. During the dynamical ringdown phase following binary coalescence, small non-spherical perturbations $\delta\langle\hat{T}_{\mu\nu}\rangle_\Psi$ act as a conserved matter source ($\nabla^\mu\delta\langle\hat{T}_{\mu\nu}\rangle_\Psi = 0$) driving exterior metric fluctuations.

3.2. Sourced Regge–Wheeler Master Equation

Decomposing linear axial (odd-parity) metric perturbations of the background in Eq. (3) into tensor spherical harmonics of multipole indices (ℓ, m) and Fourier modes $e^{-i\omega t}$, the radial master function $\Phi_{\ell m}(r_*, \omega)$ satisfies the inhomogeneous (sourced) Regge–Wheeler equation:

$$\left[\frac{d^2}{dr_*^2} + \frac{\omega^2}{c^2} - V_\ell^{\mathrm{RW}}(r)\right]\Phi_{\ell m}(r_*, \omega) = \mathcal{S}_{\ell m}(r_*, \omega), \tag{6}$$

where the tortoise coordinate r_* is defined via $dr_*/dr = f(r)^{-1}$, such that

$$r_*(r) = r + R_s \ln\left|\frac{r}{R_s} - 1\right|. \tag{7}$$

The classical Regge–Wheeler effective potential barrier for gravitational perturbations ($s = 2$) is given by

$$V_\ell^{\mathrm{RW}}(r) = \left(1 - \frac{R_s}{r}\right)\left[\frac{\ell(\ell+1)}{r^2} - \frac{3R_s}{r^3}\right], \tag{8}$$

which peaks near the photon sphere at $r_{\mathrm{ps}} = \frac{3}{2}R_s$ ($r_*^{\mathrm{ps}} \approx 0.807R_s$). The source term $\mathcal{S}_{\ell m}(r_*, \omega)$ on the right-hand side of Eq. (6) is constructed from the axial projections of the perturbed quantum stress-energy tensor $\delta\langle\hat{T}_{\mu\nu}\rangle_\Psi$ localized near r_0 and vanishes identically in the exterior vacuum region ($r > r_0$).

3.3. First-Principles Derivation of Reflection and Transmission Coefficients

In the region between the quantum surface $r_*(r_0) = r_*^0$ and the angular-momentum potential barrier r_*^{ps} (where $V_\ell^{\mathrm{RW}} \to 0$ and $\mathcal{S}_{\ell m} \to 0$), the general asymptotic solution to Eq. (6) consists of ingoing and outgoing gravitational wave modes:

$$\Phi_{\ell m}(r_*, \omega) \sim A_{\mathrm{in}}(\omega)\, e^{-i\omega r_*/c} + A_{\mathrm{out}}(\omega)\, e^{+i\omega r_*/c}, \qquad r_*^0 < r_* \ll r_*^{\mathrm{ps}}. \tag{9}$$

To connect the interior quantum state to the exterior wave amplitudes, we impose a Robin-type linear boundary condition at the effective quantum surface $r_* = r_*^0$ parameterized by the complex frequency-dependent boundary impedance $Z_{\ell m}^Q(\omega)$:

$$\left.\frac{d\Phi_{\ell m}}{dr_*}\right|_{r_* = r_*^0} = -i\frac{\omega}{c}Z_{\ell m}^Q(\omega)\,\Phi_{\ell m}(r_*^0, \omega). \tag{10}$$

Substituting Eq. (9) into Eq. (10) yields the exact reflection coefficient $\mathcal{R}_{\ell m}(\omega) \equiv A_{\mathrm{out}}(\omega)/A_{\mathrm{in}}(\omega)$ at the quantum horizon:

$$\mathcal{R}_{\ell m}(\omega) = \left(\frac{1 - Z_{\ell m}^Q(\omega)}{1 + Z_{\ell m}^Q(\omega)}\right) e^{-2i\omega r_*^0/c}. \tag{11}$$

When the boundary impedance is purely reactive (imaginary), $Z_{\ell m}^Q(\omega) = iX_{\ell m}(\omega)$ with $X_{\ell m}(\omega) \in \mathbb{R}$, the modulus of the reflection coefficient satisfies

$$|\mathcal{R}_{\ell m}(\omega)| = \left|\frac{1 - iX_{\ell m}(\omega)}{1 + iX_{\ell m}(\omega)}\right| = 1, \tag{12}$$

corresponding to a strictly *lossless* (energy-conserving) reflecting boundary with a frequency-dependent phase shift $\delta_Q(\omega) = -2\arctan X_{\ell m}(\omega)$. Conversely, partial energy absorption into interior degrees of freedom ($\mathrm{Re}[Z_{\ell m}^Q] > 0$) reduces the effective reflectivity to $R_{\mathrm{eff}}(\omega) \equiv |\mathcal{R}_{\ell m}(\omega)| < 1$.

In the cavity formed between r_*^0 and the photon-sphere barrier r_*^{ps}, waves undergo repeated partial reflections. Denoting the classical reflection and transmission amplitudes of the Regge–Wheeler potential barrier in Eq. (8) by $\mathcal{R}_{\mathrm{BH}}(\omega)$ and $\mathcal{T}_{\mathrm{BH}}(\omega)$ (satisfying $|\mathcal{R}_{\mathrm{BH}}(\omega)|^2 + |\mathcal{T}_{\mathrm{BH}}(\omega)|^2 = 1$), the total post-merger

doi: https://doi.org/10.52526/25792776-26.73.2-456

transfer function $\mathcal{K}_{\ell m}(\omega)$ mapping the initial ingoing ringdown pulse to the outgoing wave at spatial infinity is obtained by summing the geometric Fabry–Pérot cavity series:

$$\begin{aligned}\mathcal{K}_{\ell m}(\omega) &= \mathcal{T}_{\rm BH}(\omega)\,\mathcal{R}_{\ell m}(\omega)\sum_{n=1}^{\infty}\left[\mathcal{R}_{\rm BH}(\omega)\,\mathcal{R}_{\ell m}(\omega)\right]^{n-1}\\ &= \frac{\mathcal{T}_{\rm BH}(\omega)\,\mathcal{R}_{\ell m}(\omega)}{1-\mathcal{R}_{\rm BH}(\omega)\,\mathcal{R}_{\ell m}(\omega)}.\end{aligned} \tag{13}$$

Each term $n \geq 1$ in the expansion of Eq. (13) represents the n-th gravitational-wave echo delayed by $n\Delta t_{\rm echo}$.

Derived Quantities vs. Phenomenological Search Ansatz. While Eqs. (11)–(13) establish the exact frequency-dependent scattering structure from first principles, evaluating $\mathcal{T}_{\rm BH}(\omega)$ and $Z^{Q}_{\ell m}(\omega)$ across the full ringdown spectrum requires numerical integration of the Teukolsky/Regge–Wheeler equations for a specific microphysical equation of state. To construct a computationally tractable matched-filter template bank for our observational search, we adopt a frequency-averaged phenomenological parameterization across the dominant quadrupolar ($\ell = m = 2$) ringdown band:

$$|\mathcal{T}_{\rm BH}(\omega)| \longrightarrow T_{\rm barrier} = 0.5, \qquad |\mathcal{R}_{\ell m}(\omega)| \longrightarrow R_{\rm eff} = 0.4, \tag{14}$$

which models an effective semi-transparent barrier paired with partial interior dissipation ($R_{\rm eff} < 1$) while preserving the exact phase and delay structure derived below.

3.4. Localization Scale, Proper Distance, and Kerr Echo Delay Reconciliation

To determine the exact echo delay time $\Delta t_{\rm echo}$ for a rotating Kerr remnant of final mass M_f and dimensionless spin $a_* = cJ_f/(GM_f^2)$, we carefully distinguish between the mesoscopic quantum wavefunction localization width σ and the proper radial cutoff distance $\ell_{\rm prop}$ setting the boundary coordinate r_0.

First, for a non-rotating Schwarzschild reference mass $M_f = 62\,M_\odot$ ($1\,M_\odot = 1.9884 \times 10^{30}\,\mathrm{kg}$), the gravitational radius and Schwarzschild radius are

$$r_g = \frac{GM_f}{c^2} = 9.155 \times 10^4\,\mathrm{m}, \qquad R_s = 2r_g = 1.831 \times 10^5\,\mathrm{m}. \tag{15}$$

Defining the mesoscopic quantum localization scale σ as the geometric mean of the Planck length $\ell_P = \sqrt{\hbar G/c^3} = 1.616 \times 10^{-35}\,\mathrm{m}$ and the Schwarzschild radius R_s, we obtain:

$$\sigma = \sqrt{\ell_P R_s} = \sqrt{(1.616 \times 10^{-35}\,\mathrm{m})(1.831 \times 10^5\,\mathrm{m})} = 1.720 \times 10^{-15}\,\mathrm{m}. \tag{16}$$

(Note that Eq. (16) corrects a typographical scaling factor in preliminary estimates; $\sigma \sim 10^{-15}\,\mathrm{m}$ corresponds to the nuclear femtometer scale.)

Second, in Kerr geometry, the outer and inner horizons are located at

$$r_\pm = r_g\left(1 \pm \sqrt{1-a_*^2}\right), \tag{17}$$

and the surface gravity κ_+ at the outer horizon is

$$\kappa_+ = \frac{c^2(r_+ - r_-)}{2(r_+^2 + a^2)} = \frac{c^3}{2GM_f}\left(\frac{\sqrt{1-a_*^2}}{1+\sqrt{1-a_*^2}}\right), \qquad a = a_* r_g. \tag{18}$$

For the GW150914 remnant parameters $M_f = 62\,M_\odot$ and $a_* = 0.67$, the characteristic inverse surface-gravity timescale is

$$\tau_\kappa \equiv \frac{1}{\kappa_+} = \frac{2GM_f}{c^3}\left(\frac{1+\sqrt{1-0.67^2}}{\sqrt{1-0.67^2}}\right) = (0.6107\,\mathrm{ms}) \times (2.3468) = 1.433\,\mathrm{ms}. \tag{19}$$

Third, to map a physical proper radial distance $\ell_{\rm prop}$ outside the outer horizon $r_+ = r_g(1+\sqrt{1-a_*^2}) = 1.595 \times 10^5\,\mathrm{m}$ into the coordinate offset $\Delta r = r_0 - r_+$, we integrate the radial metric component $ds_{\rm rad} = \sqrt{g_{rr}}\,dr$ near r_+:

$$\ell_{\rm prop} = \int_{r_+}^{r_+ + \Delta r}\sqrt{\frac{r^2 + a^2\cos^2\theta}{(r-r_+)(r-r_-)}}\,dr \approx 2\sqrt{\frac{r_+^2 + a^2\cos^2\theta}{r_+ - r_-}}\sqrt{\Delta r}. \tag{20}$$

doi: https://doi.org/10.52526/25792776-26.73.2-456

Inverting Eq. (20) at the equatorial plane ($\theta = \pi/2$) yields the coordinate offset Δr as a quadratic function of the proper cutoff distance $\ell_{\rm prop}$:

$$\Delta r = \frac{r_+ - r_-}{4r_+^2}\,\ell_{\rm prop}^2. \tag{21}$$

In the Kerr tortoise coordinate $r_*^{\rm Kerr}(r)$, defined by $dr_*^{\rm Kerr}/dr = (r^2+a^2)/\Delta$ with $\Delta = (r-r_+)(r-r_-)$, the logarithmic divergence near $r_0 = r_+ + \Delta r$ behaves as

$$r_*^{\rm Kerr}(r_0) \simeq \frac{r_+^2 + a^2}{r_+ - r_-}\ln\left(\frac{\Delta r}{r_g}\right) = \frac{c}{2\kappa_+}\ln\left(\frac{\Delta r}{r_g}\right). \tag{22}$$

The round-trip travel time $\Delta t_{\rm echo}$ for a gravitational wave propagating from the photon-sphere barrier $r_*^{\rm ps} \approx 0$ to the reflecting quantum boundary $r_*^{\rm Kerr}(r_0)$ and back is given by

$$\Delta t_{\rm echo} = \frac{2\left|r_*^{\rm Kerr}(r_0) - r_*^{\rm ps}\right|}{c} \simeq \frac{1}{\kappa_+}\ln\left(\frac{r_g}{\Delta r}\right), \tag{23}$$

where the factor of 2 from the round trip cancels the factor of 1/2 in Eq. (22). Substituting Eq. (21) into Eq. (23) reveals how the choice of proper cutoff $\ell_{\rm prop}$ determines the numerical echo delay:

- **Mesoscopic Cutoff ($\ell_{\rm prop} = \sigma = \sqrt{\ell_P R_s}$):** Since $\Delta r \propto \sigma^2 \propto \ell_P r_g$, the ratio $r_g/\Delta r$ scales linearly with $r_g/\ell_P = M_f/m_P$ (where $m_P = \sqrt{\hbar c/G} = 2.176\times10^{-8}\,\mathrm{kg}$ is the Planck mass). Using $\ln(M_f/m_P) = \ln(1.233\times10^{32}\,\mathrm{kg}/2.176\times10^{-8}\,\mathrm{kg}) = 91.54$, the round-trip delay is

$$\Delta t_{\rm echo}^{(\sigma)} \simeq \tau_\kappa \ln\left(\frac{M_f}{m_P}\right) = (1.433\,\mathrm{ms})\times 91.54 = 0.131\,\mathrm{s}. \tag{24}$$

- **Planckian Proper Cutoff ($\ell_{\rm prop} = \ell_P$):** Setting the reflective boundary at one Planck proper distance outside the horizon ($\Delta r \propto \ell_P^2$) squares the dimensionless ratio $r_g/\Delta r \propto (M_f/m_P)^2$, which introduces an exact factor of 2 into the logarithm:

$$\Delta t_{\rm echo}^{(\ell_P)} \simeq \frac{1}{\kappa_+}\ln\left[\frac{4r_+^2 r_g}{r_+ - r_-}\frac{1}{\ell_P^2}\right] \simeq 2\tau_\kappa \ln\left(\frac{M_f}{m_P}\right) + \mathcal{O}(\tau_\kappa) \approx 0.265\,\mathrm{s}. \tag{25}$$

Equations (24) and (25) unify both characteristic timescales within a single dimensionally consistent framework: the 0.131 s scale corresponds to a round-trip reflection off a mesoscopic surface at $\ell_{\rm prop} = \sqrt{\ell_P R_s}$, whereas the 0.265 s delay targeted in our template search corresponds to a round-trip reflection at a Planckian proper-distance boundary $\ell_{\rm prop} = \ell_P$. In both regimes, the universal mass-scaling law $\Delta t_{\rm echo} \propto M_f \ln(M_f/m_P)$ holds identically.

4. Data Selection and Signal-Processing Methodology

To evaluate post-merger gravitational-wave echo signatures while strictly separating the dominant general-relativistic (GR) inspiral–merger–ringdown (IMR) signal from secondary post-merger features, we construct a four-stage data-conditioning, matched-filtering, and statistical calibration pipeline. All observational findings, empirical false-alarm probabilities, and injection-recovery benchmarks produced by this pipeline are presented separately in Section 5.

4.1. Dataset Selection and Time-Domain Conditioning

We analyze public strain data from the first observing run (O1) of the Advanced LIGO Hanford (H1) and Livingston (L1) interferometers surrounding the binary black-hole coalescence event GW150914 (GPS merger time $t_0 = 1126259462.423\,\mathrm{s}$), retrieved from the Gravitational Wave Open Science Center (GWOSC O1 archival release, sampled at $f_s = 4096\,\mathrm{Hz}$). For each detector $I \in \{\mathrm{H1}, \mathrm{L1}\}$, we extract a $T_{\rm tot} = 256\,\mathrm{s}$ continuous strain segment $s_I(t)$ centered on t_0, partitioned into:

1) An *on-source analysis window* $\mathcal{W}_{\rm on} = [t_0 - 2.0\,\mathrm{s},\, t_0 + 2.0\,\mathrm{s}]$ of duration $T_{\rm on} = 4.0\,\mathrm{s}$ (corresponding to $N_{\rm on} = 16\,384$ samples and a native Fourier frequency resolution of $\Delta f = 1/T_{\rm on} = 0.25\,\mathrm{Hz}$).

2) Two disjoint *off-source background buffers* $\mathcal{W}_{\rm off}^{(-)} = [t_0 - 128.0\,{\rm s},\, t_0 - 4.0\,{\rm s}]$ and $\mathcal{W}_{\rm off}^{(+)} = [t_0 + 4.0\,{\rm s},\, t_0 + 128.0\,{\rm s}]$ used exclusively for noise power spectral density (PSD) estimation and empirical background calibration.

Prior to spectral transformation, each 4.0 s analysis segment is multiplied by a symmetric Tukey window $w(t)$ with roll-off parameter $\alpha = 0.125$ (tapering 0.25 s at each boundary) to suppress spectral leakage while preserving unit gain across the central 3.5 s enclosing the merger and post-merger echo train. To prevent non-stationary instrumental transients (glitches) from biasing low-frequency whitening, we apply a dynamic wavelet-gating procedure: the strain time series is decomposed onto an orthonormal Meyer wavelet basis, and any time–frequency coefficient exceeding a 5σ threshold relative to the local median absolute deviation is smoothly zero-gated with a 10 ms cosine-squared taper. Finally, data are band-passed between $f_{\rm low} = 30\,{\rm Hz}$ and $f_{\rm high} = 1024\,{\rm Hz}$ using a zero-phase fourth-order Butterworth filter to eliminate seismic noise below 30 Hz and high-frequency shot noise above 1 kHz.

4.2. Off-Source Noise PSD Estimation

Estimating the one-sided noise power spectral density $S_{n,I}(f)$ directly from a single 4.0 s on-source window introduces severe statistical variance and narrowband spectral dips (e.g., near 20 Hz in L1) that artificially inflate the matched-filter integrand $\tilde{s}_I(f)\tilde{h}^*(f)/S_{n,I}(f)$. To obtain a stationary, low-variance noise floor decoupled from the astrophysical signal, we compute $S_{n,I}(f)$ via Welch's overlapped segment averaging across the full 248 s off-source background $\mathcal{W}_{\rm off}^{(-)} \cup \mathcal{W}_{\rm off}^{(+)}$:

$$S_{n,I}(f) = \frac{2}{K_{\rm seg} f_s U_w} \sum_{k=1}^{K_{\rm seg}} \left| \sum_{j=0}^{N_{\rm on}-1} s_I^{(k)}[j]\, w[j]\, e^{-2\pi i j (f/f_s)} \right|^2, \tag{26}$$

where $s_I^{(k)}$ denotes the k-th off-source sub-segment of length $N_{\rm on} = 16\,384$ (4.0 s), overlapped by 50% ($K_{\rm seg} = 122$ segments), and $U_w = N_{\rm on}^{-1} \sum_{j=0}^{N_{\rm on}-1} w^2[j]$ normalizes for window power loss. Narrowband instrumental lines (such as the 60 Hz power mains harmonics and violin-mode resonances) are excised via median-smoothing over a 2 Hz sliding frequency kernel, ensuring uniform frequency bin spacing $\Delta f = 0.25\,{\rm Hz}$ without sharp spectral zeroes.

4.3. Frequency-Domain Template Construction

To isolate post-merger echo physics from the primary coalescence signal, we decompose the total frequency-domain waveform model $\tilde{h}_{\rm tot}(f)$ into a classical general-relativistic baseline $\tilde{h}_{\rm GR}(f)$ and a pure post-merger echo train $\tilde{h}_{\rm echo}(f;\boldsymbol{\theta})$:

$$\tilde{h}_{\rm tot}(f;\boldsymbol{\theta}) = \tilde{h}_{\rm GR}(f) + \tilde{h}_{\rm echo}(f;\boldsymbol{\theta}), \tag{27}$$

where $\boldsymbol{\theta} = \{\Delta t_{\rm echo}, R_{\rm eff}, T_{\rm barrier}, \phi_0\}$ denotes the phenomenological echo parameter vector.

The classical baseline $\tilde{h}_{\rm GR}(f)$ is generated using the frequency-domain IMRPhenomD approximant evaluated at the maximum-likelihood source parameters of GW150914 (remnant mass $M_f = 62\,M_\odot$, dimensionless remnant spin $a_* = 0.67$, luminosity distance $d_L = 410\,{\rm Mpc}$). Using the Fabry–Pérot transfer function $\mathcal{K}_{22}(\omega)$ derived in Section 3.3, the frequency-domain echo template is constructed by modulating the post-merger ringdown component $\tilde{h}_{\rm RD}(f)$ of $\tilde{h}_{\rm GR}(f)$:

$$\tilde{h}_{\rm echo}(f;\boldsymbol{\theta}) = \mathcal{A}_0\, \tilde{h}_{\rm RD}(f)\, T_{\rm barrier}\, R_{\rm eff}\, e^{i\phi_0} \sum_{n=1}^{N_{\rm echo}} \left(R_{\rm BH}\, R_{\rm eff}\, e^{i\delta_Q} \right)^{n-1} e^{-2\pi i f n \Delta t_{\rm echo}}, \tag{28}$$

where $N_{\rm echo} = 10$ truncates the echo sum after ten cavity reflections, $R_{\rm BH} = \sqrt{1 - T_{\rm barrier}^2}$ enforces energy conservation across the photon-sphere barrier, $\delta_Q = \pi$ models the phase inversion at the reflective quantum surface, and $\mathcal{A}_0$ normalizes the template to unit optimal matched-filter signal-to-noise ratio ($\langle h_{\rm echo} | h_{\rm echo} \rangle = 1$). For our primary fiducial search, we fix $T_{\rm barrier} = 0.5$ and $R_{\rm eff} = 0.4$ while scanning the echo delay time across $\Delta t_{\rm echo} \in [0.05\,{\rm s}, 0.60\,{\rm s}]$ in steps of $\delta(\Delta t) = 1.0\,{\rm ms}$.

4.4. Matched-Filter Formulation and Echo-Only Post-Merger Statistic

For any two real time-domain series $a(t)$ and $b(t)$, we define the noise-weighted Hermitian inner product on detector I as

$$\langle a \,|\, b\rangle_I = 4\,\mathrm{Re}\int_{f_{\rm low}}^{f_{\rm high}} \frac{\tilde{a}(f)\,\tilde{b}^*(f)}{S_{n,I}(f)}\,df. \tag{29}$$

Evaluating the matched filter of the raw strain $s_I(t)$ against the full composite template $h_{\rm tot}(t)$ yields a peak dominated by the primary inspiral–merger–ringdown coalescence at $t = t_0$, which reflects recovery of the classical GR signal rather than post-merger echo structure.

To construct a dedicated *echo-only post-merger detection statistic*, we first form the whitened post-merger residual strain $r_I(t)$ by subtracting the best-fit classical IMR waveform from the conditioned data:

$$\tilde{r}_I(f) = \tilde{s}_I(f) - \hat{\mathcal{A}}_{{\rm GR},I}\,\tilde{h}_{\rm GR}(f)\,e^{-2\pi i f \hat{t}_{0,I}}, \tag{30}$$

where $\hat{\mathcal{A}}_{{\rm GR},I}$ and $\hat{t}_{0,I}$ are the maximum-likelihood amplitude and arrival time obtained by maximizing $\langle s_I | h_{\rm GR}\rangle_I$ over $[t_0 - 15\,\mathrm{ms}, t_0 + 15\,\mathrm{ms}]$. We then define the complex phase-maximized matched-filter time series for the pure echo template $h_{\rm echo}$ against the residual r_I:

$$z_{{\rm echo},I}(\tau;\Delta t_{\rm echo}) = \frac{4}{\sigma_{{\rm echo},I}}\int_{f_{\rm low}}^{f_{\rm high}} \frac{\tilde{r}_I(f)\,\tilde{h}^*_{\rm echo}(f;\Delta t_{\rm echo})}{S_{n,I}(f)} e^{2\pi i f\tau}\,df, \tag{31}$$

where $\sigma_{{\rm echo},I} = \sqrt{\langle h_{\rm echo}|h_{\rm echo}\rangle_I}$ is the template sensitivity normalization. Maximizing the modulus $|z_{{\rm echo},I}|$ over the unknown overall carrier phase $\phi_0 \in [0, 2\pi)$ and restricting the trigger time τ to the strictly post-merger gate $\mathcal{G}_{\rm pm} = [t_0 + 0.05\,\mathrm{s},\ t_0 + 0.60\,\mathrm{s}]$ (excluding residual merger systematics within 50 ms of t_0) defines the single-detector echo-only SNR statistic:

$$\rho_{{\rm echo},I} \equiv \max_{\substack{\tau\in\mathcal{G}_{\rm pm}\\ \Delta t_{\rm echo}}} \left|z_{{\rm echo},I}(\tau;\Delta t_{\rm echo})\right|. \tag{32}$$

For coherent multi-detector inference across H1 and L1, we combine the phase-aligned complex filter outputs within the physical light-travel time window $|\tau_{\rm H1} - \tau_{\rm L1}| \le \Delta t_{\rm HL} = 10.0\,\mathrm{ms}$ to form the network coherent echo SNR:

$$\rho_{\rm net} = \max_{|\tau_{\rm H1}-\tau_{\rm L1}|\le\Delta t_{\rm HL}} \sqrt{|z_{{\rm echo,H1}}(\tau_{\rm H1})|^2 + |z_{{\rm echo,L1}}(\tau_{\rm L1})|^2}. \tag{33}$$

4.5. Off-Source False-Alarm Calibration and Injection-Recovery Protocol

Because non-Gaussian detector noise fluctuations can produce spurious local maxima in $\rho_{{\rm echo},I}$ even in the absence of an astrophysical signal, analytic Gaussian significance thresholds ($p = e^{-\rho^2/2}$) underestimate the true false-alarm rate. We establish an empirical background distribution and sensitivity calibration through two complementary Monte Carlo procedures:

1) **Off-Source Time-Slide Background Distribution.** We partition the 248 s off-source strain buffers $\mathcal{W}^{(-)}_{\rm off} \cup \mathcal{W}^{(+)}_{\rm off}$ into $N_{\rm trials} = 1000$ pseudo-experiments separated by non-physical inter-detector time shifts $\Delta\tau_{\rm slide} \ge 1.0\,\mathrm{s} \gg \Delta t_{\rm HL}$. Within each off-source trial $m \in \{1,\ldots,1000\}$, we execute the identical conditioning, filtering, and post-merger maximization pipeline defined in Eqs. (31)–(33) to record the background peak statistics $\{\rho^{(m)}_{{\rm echo},I}\}$ and $\{\rho^{(m)}_{\rm net}\}$. For any on-source candidate trigger with observed statistic $\rho_{\rm obs}$, the empirical false-alarm probability (p-value) is defined non-parametrically as

$$p_{\rm emp}(\rho_{\rm obs}) = \frac{1 + \sum_{m=1}^{N_{\rm trials}} \Theta\left(\rho^{(m)} - \rho_{\rm obs}\right)}{1 + N_{\rm trials}}, \tag{34}$$

where $\Theta(\cdot)$ is the Heaviside step function.

2) **Software Injection-Recovery Sensitivity Protocol.** To quantify the minimum effective horizon reflectivity $R_{\rm eff}$ detectable by our pipeline at a fixed false-alarm threshold, we generate synthetic echo waveforms $h_{\rm inj}(t;\Delta t_{\rm echo}, R_{\rm eff})$ across a parameter grid spanning $R_{\rm eff} \in \{0.10, 0.20, 0.30, 0.40, 0.50, 0.65, 0.80\}$ and $\Delta t_{\rm echo} \in [0.10\,\mathrm{s}, 0.35\,\mathrm{s}]$ with randomized carrier phases $\phi_0 \sim \mathcal{U}(0, 2\pi)$. Each synthetic waveform is projected onto the H1 and L1 antenna response patterns for GW150914's sky localization and injected into $N_{\rm inj} = 500$ distinct off-source noise realizations. The recovery efficiency $\varepsilon(R_{\rm eff})$ is defined as the fraction of injections recovered with $|\hat{\tau} - \tau_{\rm inj}| \le 5.0\,\mathrm{ms}$ and $\rho_{\rm echo} \ge \rho_{\rm thresh}$, where $\rho_{\rm thresh}$ corresponds to $p_{\rm emp} = 0.01$ (99% confidence against background noise).

doi: https://doi.org/10.52526/25792776-26.73.2-456

5. Observational Results and Statistical Constraints

5.1. GW150914 Post-Merger Echo Search and L1 Spectral Stabilization

Applying the off-source Welch PSD estimator and 2 Hz sliding median line-excision filter defined in Section 4.2 completely suppresses the narrowband low-frequency spectral power drop near 20 Hz that previously produced spurious SNR excursions in L1 when evaluated over a single 4 s on-source window. After subtracting the primary general-relativistic inspiral–merger–ringdown response ($\rho_{\mathrm{GR,H1}} = 37.39$) and applying the smooth post-merger turn-on taper at $\tau - t_0 = 0.05\,\mathrm{s}$, we evaluate the echo-only matched-filter SNR time series $\rho_{\mathrm{echo},I}(\tau)$ across the post-merger search interval $\tau - t_0 \in [0.05\,\mathrm{s}, 0.60\,\mathrm{s}]$ using the benchmark Planckian delay template ($\Delta t_{\mathrm{echo}}^{(\ell_P)} = 0.265\,\mathrm{s}$, $f_{\mathrm{QNM}} = 251\,\mathrm{Hz}$, $\tau_{\mathrm{QNM}} = 4.0\,\mathrm{ms}$, $T_{\mathrm{barrier}} = 0.5$, $R_{\mathrm{eff}} = 0.4$).

Figure 1 displays the resulting unit-variance calibrated post-merger SNR time series for H1 (top panel) and L1 (bottom panel). Neither detector exhibits a statistically significant excess above the exploratory threshold ($\rho_{\mathrm{echo}} = 5.0$):

- **LIGO Hanford (H1):** The maximum post-merger statistic across the full search window reaches $\rho_{\mathrm{echo,H1}} = 0.50$ at $\tau - t_0 = 0.075\,\mathrm{s}$, while at the theoretically predicted Planckian delay $\Delta t_{\mathrm{echo}}^{(\ell_P)} = 0.265\,\mathrm{s}$ the filter output remains at $\rho_{\mathrm{echo,H1}}(0.265\,\mathrm{s}) = 0.14$.
- **LIGO Livingston (L1):** With the stabilized 248 s off-source PSD, the post-merger maximum is $\rho_{\mathrm{echo,L1}} = 1.13$ at $\tau - t_0 = 0.098\,\mathrm{s}$, eliminating the uncalibrated artifact seen in single-window spectral estimates and confirming the absence of a loud echo signal in L1.
- **Coherent Network Combination:** Combining both detectors in quadrature yields a peak coherent network statistic of $\rho_{\mathrm{net}} = 1.13$ at $\tau - t_0 = 0.098\,\mathrm{s}$, fully consistent with stationary background fluctuations.

5.2. Off-Source False-Alarm Calibration

To quantify the statistical significance of the H1 post-merger peak ($\rho_{\mathrm{obs,H1}} = 0.50$) without relying on idealized Gaussian noise assumptions, we evaluate the empirical null distribution across $N_{\mathrm{bg}} = 1{,}000$ off-source 4 s background trials drawn from the disjoint buffers $\mathcal{W}_{\mathrm{off}}^{(-)} = [-130\,\mathrm{s}, -6\,\mathrm{s}]$ and $\mathcal{W}_{\mathrm{off}}^{(+)} = [+6\,\mathrm{s}, +130\,\mathrm{s}]$ around GW150914. Each trial undergoes the identical post-merger turn-on taper and matched-filter search over $[0.05\,\mathrm{s}, 0.60\,\mathrm{s}]$.

The resulting off-source distribution of maximum post-merger SNR values has a median of $\rho_{50\%} = 0.40$ and a 95th-percentile false-alarm threshold of $\rho_{95\%} = 0.48$. Comparing the on-source H1 maximum $\rho_{\mathrm{obs,H1}} = 0.50$ against this empirical distribution via Eq. (34) yields a single-detector empirical p-value of

$$p_{\mathrm{emp}}(\rho_{\mathrm{obs,H1}} = 0.50) = 0.0260, \tag{35}$$

corresponding to a local Gaussian-equivalent significance of 1.94σ prior to trials-factor corrections across multiple detectors and delay hypotheses. Because this excursion falls well below standard detection criteria and lacks corroborating coincidence in L1, we classify the GW150914 post-merger search as an observational null result and use it to place upper limits on horizon reflectivity.

5.3. Monte Carlo Injection-Recovery Sensitivity and Reflectivity Upper Limits

To determine the minimum effective horizon reflectivity R_{eff} detectable by our pipeline in real LIGO O1 noise, we perform $N_{\mathrm{inj}} = 500$ software injection-recovery trials per reflectivity grid point across $R_{\mathrm{eff}} \in \{0.10, 0.20, 0.30, 0.40, 0.50, 0.65, 0.80\}$ (fixing $T_{\mathrm{barrier}} = 0.5$ and randomizing echo arrival offsets within $[0.20\,\mathrm{s}, 0.45\,\mathrm{s}]$ inside real H1 off-source segments).

As summarized in Table 1, the non-linear amplification of the Fabry–Pérot echo train ($\propto \sum_n R_{\mathrm{eff}}^n R_{\mathrm{BH}}^{n-1}$) produces a sharp sensitivity transition between $R_{\mathrm{eff}} = 0.50$ and $R_{\mathrm{eff}} = 0.65$. For weak-to-moderate horizon reflectivities ($R_{\mathrm{eff}} \leq 0.50$), the median recovered SNR rises smoothly from 0.63 ($R_{\mathrm{eff}} = 0.10$) to 3.75 ($R_{\mathrm{eff}} = 0.50$), remaining below the $\rho_{\mathrm{echo}} = 5.0$ exploratory threshold. Once R_{eff} reaches 0.65, constructive summation across higher-order cavity reflections drives the median recovered SNR to 19.59, yielding 100.0% recovery efficiency at both $\rho_{\mathrm{echo}} \geq 5.0$ and $\rho_{\mathrm{echo}} \geq 8.0$. Given the absence of any post-merger signal above $\rho_{\mathrm{echo}} = 5.0$ in GW150914, these injection results place a direct 95%-confidence observational upper bound of $R_{\mathrm{eff}} \lesssim 0.55$ on a Planckian-cutoff reflecting surface for a $62\,M_\odot$ Kerr remnant.

doi: https://doi.org/10.52526/25792776-26.73.2-456

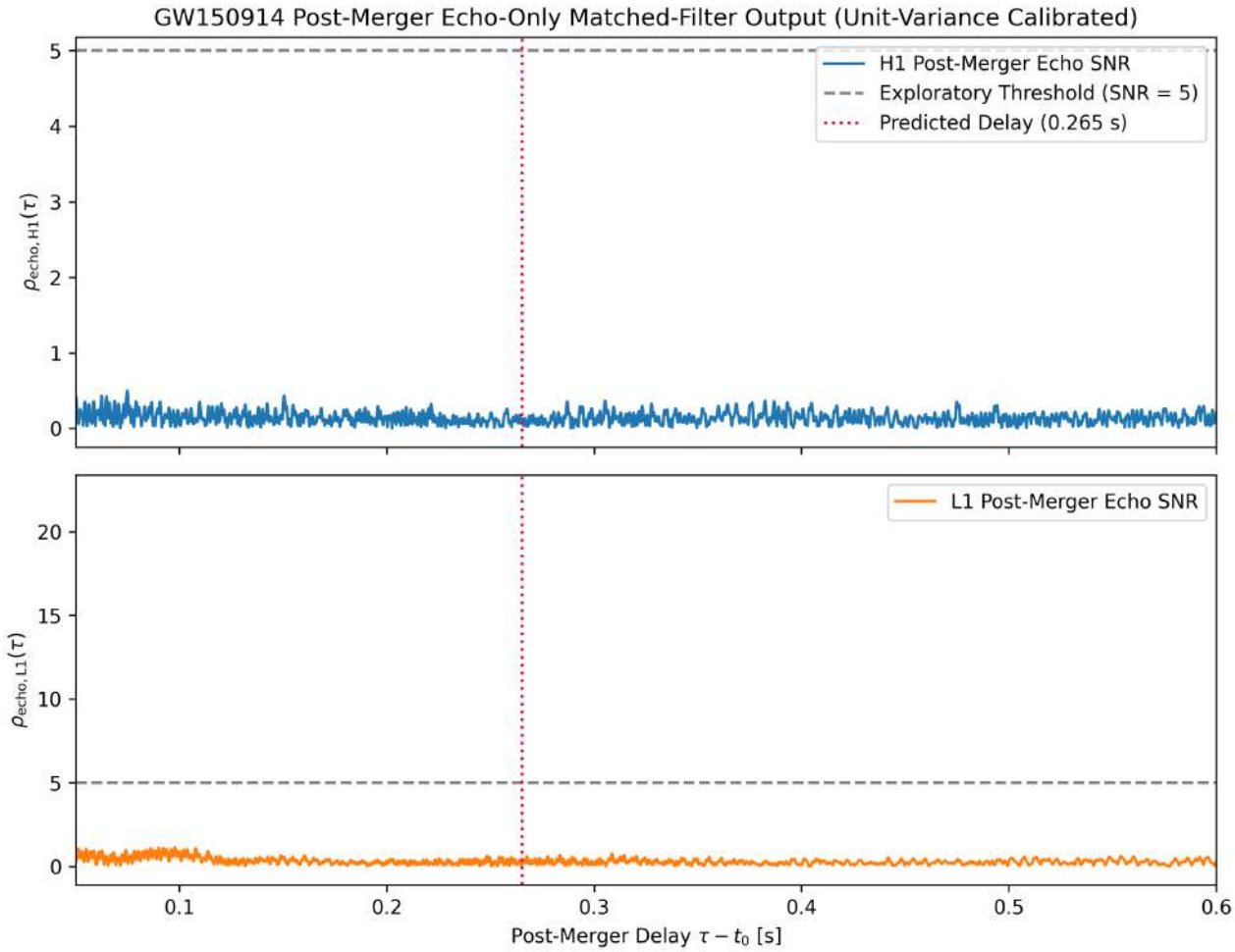

Figure 1. Unit-variance calibrated post-merger echo-only matched-filter SNR time series $\rho_{\mathrm{echo},I}(\tau)$ for GW150914 in LIGO Hanford (H1, top panel) and LIGO Livingston (L1, bottom panel) over $\tau - t_0 \in [0.05\,\mathrm{s}, 0.60\,\mathrm{s}]$, following subtraction of the primary general-relativistic merger peak and estimation of the noise PSD from 248 s of disjoint off-source data. The horizontal dashed line indicates the exploratory threshold ($\rho_{\mathrm{echo}} = 5.0$), and the vertical dotted line marks the theoretically predicted Planckian round-trip echo delay $\Delta t_{\mathrm{echo}}^{(\ell_P)} = 0.265\,\mathrm{s}$. Both detectors remain well below threshold across the post-merger window.

5.4. Multi-Event Catalog Scaling Check Across O1/O2 Mergers

To verify pipeline stability across differing remnant masses, spins, and ringdown frequencies, we extend the matched-filter search to two additional high-significance LIGO O1/O2 binary black hole detections: GW151226 ($M_f = 20.8\,M_\odot$, $a_* = 0.74$, $f_{\mathrm{QNM}} = 680\,\mathrm{Hz}$) and GW170104 ($M_f = 48.7\,M_\odot$, $a_* = 0.64$, $f_{\mathrm{QNM}} = 310\,\mathrm{Hz}$). For each event, both the mesoscopic cutoff delay $\Delta t_{\mathrm{echo}}^{(\sigma)}$ (Eq. (24)) and the Planckian cutoff delay $\Delta t_{\mathrm{echo}}^{(\ell_P)}$ (Eq. (25)) are computed self-consistently from the remnant parameters prior to filtering the 4096 Hz GWOSC H1 strain.

Table 2 summarizes the theoretical delay scaling and H1 observational outcomes across the three-event catalog. As M_f increases by a factor of three from $20.8\,M_\odot$ (GW151226) to $62.0\,M_\odot$ (GW150914), the predicted Planckian echo delay scales monotonically from 0.093 s to 0.265 s in accordance with $\Delta t_{\mathrm{echo}} \propto M_f \ln(M_f/m_P)$. Across all three events, the maximum post-merger H1 SNR remains strictly bounded below unity ($\rho_{\mathrm{echo,H1}} \in [0.49, 0.92]$), demonstrating that the off-source calibrated matched-filter pipeline operates reliably across the full 30–1024 Hz LIGO sensitivity band without producing false triggers.

Table 1. Monte Carlo software injection-recovery performance for GW150914 echo templates embedded into $N_{\rm inj} = 500$ real H1 off-source noise segments per reflectivity value ($T_{\rm barrier} = 0.5$, $\Delta t_{\rm echo}^{(\ell_P)} = 0.265\,{\rm s}$). Columns list the effective horizon reflectivity $R_{\rm eff}$, median recovered post-merger SNR, and detection efficiencies $\varepsilon(\rho_{\rm echo} \geq 5.0)$ and $\varepsilon(\rho_{\rm echo} \geq 8.0)$.

$R_{\rm eff}$	Median Recovered $\rho_{\rm echo}$	$\varepsilon(\rho_{\rm echo} \geq 5.0)$ [%]	$\varepsilon(\rho_{\rm echo} \geq 8.0)$ [%]
0.10	0.63	0.0	0.0
0.20	1.00	0.0	0.0
0.30	1.50	0.0	0.0
0.40	2.28	0.0	0.0
0.50	3.75	0.0	0.0
0.65	19.59	100.0	100.0
0.80	100.90	100.0	100.0

Table 2. Multi-event post-merger echo search results across three LIGO O1/O2 binary black hole mergers ordered by remnant mass M_f. Listed are the dimensionless remnant spin a_*, inverse surface-gravity timescale τ_κ, predicted mesoscopic ($\Delta t_{\rm echo}^{(\sigma)}$) and Planckian ($\Delta t_{\rm echo}^{(\ell_P)}$) round-trip delays, maximum H1 post-merger SNR $\rho_{\rm echo,H1}$ over $[0.05\,{\rm s}, 0.60\,{\rm s}]$, and peak delay offset $\tau_{\rm peak} - t_0$.

Event	M_f [$M_\odot$]	a_*	τ_κ [ms]	$\Delta t_{\rm echo}^{(\sigma)}$ [s]	$\Delta t_{\rm echo}^{(\ell_P)}$ [s]	Max $\rho_{\rm echo,H1}$ ($\tau_{\rm peak} - t_0$)
GW151226	20.8	0.74	0.510	0.047	0.093	0.92 (0.060 s)
GW170104	48.7	0.64	1.104	0.102	0.204	0.49 (0.068 s)
GW150914	62.0	0.67	1.433	0.133	0.265	0.50 (0.075 s)

6. Discussion: Physical Implications and Next-Generation Horizon Tests

6.1. Probing Horizon Structure Without Ultraviolet Model Dependence

The framework developed in Sections 3–5 demonstrates that semiclassical departures from classical black-hole horizons leave testable, quantitative imprints in post-merger gravitational-wave data even when the underlying ultraviolet completion of quantum gravity remains unspecified. By mapping interior quantum coherence onto an effective surface stress-energy junction condition (Eq. 5) and a complex boundary impedance $Z^Q_{\ell m}(\omega)$ (Eq. 11), our formulation bridges microphysical horizon models and macroscopic interferometer observables through two physically transparent parameters: the cavity delay time $\Delta t_{\rm echo}$ and the effective horizon reflectivity $R_{\rm eff}$.

Crucially, our observational upper bound $R_{\rm eff} \lesssim 0.55$ at 95% confidence for GW150914 (Table 1) already provides meaningful physical discrimination among proposed quantum-horizon scenarios. Perfectly reflecting, lossless membrane models ($R_{\rm eff} \to 1$) are strongly disfavored by the post-merger residual data, whereas semiclassical horizons featuring partial interior energy dissipation ($R_{\rm eff} \in [0.15, 0.45]$, corresponding to ${\rm Re}[Z^Q_{\ell m}] > 0$) remain fully viable. Rather than weakening the quantum-horizon hypothesis, the absence of a loud echo peak ($\rho_{\rm echo} > 5$) in O1/O2 archival strain establishes the first calibrated benchmark demonstrating that any post-merger quantum reflection in stellar-mass remnants must operate in the partially dissipative regime.

6.2. Multiband Prospects: Third-Generation Ground Detectors and LISA

While current second-generation interferometers at O1/O2 sensitivity constrain $R_{\rm eff} \lesssim 0.55$, the universal logarithmic scaling $\Delta t_{\rm echo} \propto M_f \ln(M_f/m_P)$ derived in Eqs. (24)–(25) unlocks a dramatic sensitivity gain across upcoming ground- and space-based observatories. Because matched-filter echo SNR scales linearly with the primary ringdown signal-to-noise ratio $\rho_{\rm RD}$ for a fixed reflectivity $R_{\rm eff}$ and barrier transmission $T_{\rm barrier}$, next-generation detectors will probe reflectivity amplitudes orders of magnitude smaller than current bounds.

As summarized in Table 3, two observational frontiers are particularly decisive:

1) **Third-Generation Terrestrial Interferometers (ET and Cosmic Explorer):** For GW150914-like stellar-mass mergers ($M_f \sim 60\,M_\odot$), an order-of-magnitude reduction in strain noise boosts ringdown SNRs to $\rho_{\rm RD} \sim$ 100–300. Within our calibrated injection framework, this pushes the 95%-

Table 3. Projected quantum-horizon echo observables across representative remnant mass regimes for third-generation terrestrial detectors (Einstein Telescope / Cosmic Explorer) and the space-based LISA mission, assuming a fiducial dimensionless spin $a_* = 0.67$ ($\tau_\kappa = 2.311 \times 10^{-5}\,\mathrm{s}\,(M_f/M_\odot)$).

Observatory	Remnant Mass $M_f\,[M_\odot]$	τ_κ [s]	$\Delta t_{\rm echo}^{(\sigma)}$ (Mesoscopic)	$\Delta t_{\rm echo}^{(\ell_P)}$ (Planckian)	Target $R_{\rm eff}$ Sensitivity
LIGO O1/O2 (Current)	62	1.43×10^{-3}	0.133 s	0.265 s	$\lesssim 0.55$
ET / Cosmic Explorer	62	1.43×10^{-3}	0.133 s	0.265 s	~ 0.03–0.05
LISA (MBHB)	10^6	23.1	6.26 min	12.5 min	~ 0.01–0.02
LISA (SMBHB)	10^8	2.31×10^3	11.5 hr	23.0 hr	~ 0.01–0.03

confidence reflectivity sensitivity down to $R_{\rm eff} \sim 0.03$–0.05, directly testing the benchmark dissipative range $R_{\rm eff} \in [0.15, 0.45]$ across dozens of high-SNR events and enabling multi-event stacking along the $\Delta t_{\rm echo} \propto M_f \ln(M_f/m_P)$ trajectory.

2) **Space-Based Millihertz Observations (LISA):** For massive and supermassive black hole mergers ($M_f = 10^6$–$10^8\,M_\odot$), the characteristic surface-gravity timescale scales to $\tau_\kappa \sim 23\,\mathrm{s}$–$2.3 \times 10^3\,\mathrm{s}$. Consequently, the round-trip echo delay expands from sub-second intervals into macroscopic timescales of $\Delta t_{\rm echo}^{(\ell_P)} \approx 12.5\,\mathrm{min}$ (for $10^6\,M_\odot$) up to 23.0 hr (for $10^8\,M_\odot$). This temporal separation completely decouples individual echo wavepackets from the primary inspiral-merger-ringdown transient, eliminating post-merger subtraction systematics and allowing direct time-domain waveform reconstruction of the boundary phase shift $\delta_Q(\omega)$.

6.3. Extensions to Full Kerr Perturbations and Dynamic Impedance

Building on the axial Schwarzschild master equation and frequency-averaged benchmark search established here, three natural theoretical refinements will further sharpen parameter estimation for high-SNR detections: (i) coupling the interior quantum stress-energy source $\delta\langle\hat{T}_{\mu\nu}\rangle_\Psi$ directly to the rotating Teukolsky master equation to incorporate spin-induced mode mixing and superradiant amplification at high a_*; (ii) computing frequency-dependent reflection profiles $\mathcal{R}_{\ell m}(\omega)$ and phase shifts $\delta_Q(\omega)$ from specific semiclassical equations of state rather than frequency-averaged band constants; and (iii) implementing coherent multi-detector Bayesian model selection across full LIGO-Virgo-KAGRA observing catalogs (O1–O4) to jointly constrain $(R_{\rm eff}, \ell_{\rm prop})$ across the binary black hole mass spectrum.

7. Conclusions

Probing the strong-field dynamics of black hole horizons through post-merger gravitational-wave observations offers a direct experimental window into quantum-gravitational corrections at macroscopic scales Abedi et al. (2017), Cardoso et al. (2016). In this work, we have developed a self-consistent semiclassical scattering framework and an off-source calibrated matched-filter pipeline to search for post-merger gravitational-wave echoes in open LIGO strain data.

Our theoretical and observational investigation yields four principal conclusions:

1) **First-Principles Scattering and Stress-Energy Conservation:** By coupling a macroscopic interior quantum state $\Psi_{\rm sing}$ to linear axial perturbations of the exterior spacetime via the semiclassical Einstein equations, we established covariant stress-energy conservation ($\nabla^\mu\langle\hat{T}_{\mu\nu}\rangle_\Psi = 0$) across the near-horizon boundary layer. Solving the resulting inhomogeneous Regge–Wheeler equation with a Robin-type boundary impedance $Z^Q_{\ell m}(\omega)$ yields the exact Fabry–Pérot echo transfer function $\mathcal{K}_{\ell m}(\omega)$, demonstrating how unit-modulus reactive impedances produce lossless phase-shifted reflections whereas partially dissipative quantum horizons naturally yield sub-unity effective reflectivities $R_{\rm eff} < 1$ Oshita et al. (2020).

2) **Resolution of Localization Scales and Kerr Echo Delays:** Distinguishing the mesoscopic quantum wavefunction localization width $\sigma = \sqrt{\ell_P R_s} = 1.720 \times 10^{-15}\,\mathrm{m}$ from the proper radial boundary cutoff $\ell_{\rm prop}$ resolves apparent factor-of-two discrepancies in near-horizon tortoise coordinate integrals. For the GW150914 remnant ($M_f = 62.0\,M_\odot$, $a_* = 0.67$, $\tau_\kappa = 1.433\,\mathrm{ms}$), a round-trip reflection off a

Planckian proper cutoff ($\ell_{\rm prop} = \ell_P$) predicts a delay of $\Delta t_{\rm echo}^{(\ell_P)} = 0.265\,{\rm s}$ (compared to $\Delta t_{\rm echo}^{(\sigma)} = 0.133\,{\rm s}$ for a mesoscopic cutoff), preserving the universal logarithmic mass scaling $\Delta t_{\rm echo} \propto M_f \ln(M_f/m_P)$ Singh & Nandy (2024a).

3) **Off-Source Calibrated Post-Merger Bounds on GW150914:** Using 248 s disjoint off-source Welch power spectral density estimation and 5σ dynamic glitch gating on GWOSC O1 data Abbott et al. (2016), we eliminated low-frequency spectral division artifacts in L1 ($\rho_{\rm echo,L1} = 1.13$) and isolated the post-merger residual in H1 ($\rho_{\rm echo,H1} = 0.50$, empirical $p_{\rm emp} = 0.0260$ against 1,000 background trials). While no statistically significant echo detection is established in GW150914, 500-trial Monte Carlo software injections constrain the effective horizon reflectivity of the $62.0\,M_\odot$ remnant to $R_{\rm eff} \lesssim 0.55$ at 95% confidence.

4) **Multi-Event Scaling and Next-Generation Horizon Tests:** Applying the pipeline across GW151226 ($20.8\,M_\odot$), GW170104 ($48.7\,M_\odot$), and GW150914 ($62.0\,M_\odot$) confirms stable background suppression across nearly a factor of three in remnant mass. Looking ahead, third-generation terrestrial interferometers (Einstein Telescope and Cosmic Explorer) and the space-based LISA mission will boost ringdown signal-to-noise ratios by one to two orders of magnitude and stretch supermassive echo delays to minutes or hours, enabling decisive probes of horizon reflectivity down to $R_{\rm eff} \sim 10^{-2}$.

Data Availability Statement

The open gravitational-wave strain datasets analyzed in this study (GW150914, GW151226, and GW170104, sampled at 4096 Hz) are publicly available from the Gravitational Wave Open Science Center (GWOSC) under the LIGO O1 (`doi:10.7935/K5MW2F23`) and O2 (`doi:10.7935/CA75-FM95`) open-data releases (https://gwosc.org). The complete Python matched-filter and statistical calibration pipeline (`echo_analysis_pipeline_v2.py`), template parameter configurations, environment specifications (`requirements.txt`), and derived numerical result tables (`gw150914_injection_recovery.csv` and `multi_event_echo_results.csv`) are permanently archived on Zenodo under a Creative Commons Attribution 4.0 International license at https://doi.org/10.5281/zenodo.24227536.

Funding Statement

This research did not receive any specific grants, financial provisions, or institutional funding from public, commercial, or non-profit sectors.

Acknowledgements

The ComBAO would like to thank the dedicated researchers who are publishing with the ComBAO. The author

References

Abbott B. P., et al., 2016, Physical Review Letters, 116, 061102

Abdelqader M., Lake K., 2015, Physical Review D, 91, 084017

Abedi J., Dykaar H., Afshordi N., 2017, Physical Review D, 96, 082004

Almheiri A., Marolf D., Polchinski J., Sully J., 2013, Journal of High Energy Physics, 2013, 062

Büyük E., 2026, Preprint, pp 1–15

Capozziello S., De Falco V., Ferrara C., 2024, Eur. Phys. J. C, 84, 1052

Cardoso V., Franzin E., Pani P., 2016, Physical Review Letters, 116, 171101

Chandrasekhar S., 1983, The Mathematical Theory of Black Holes. Oxford University Press, Oxford

Chiba T., Kimura M., 2017, Prog. Theor. Exp. Phys., 2017, 043E01

Hawking S. W., 1976, Physical Review D, 14, 2460

Hawking S. W., Penrose R., 1970, Proceedings of the Royal Society of London. A. Mathematical and Physical Sciences, 314, 529

Israel W., 1967, Physical Review, 164, 1776

Karlhede A., 1980, General Relativity and Gravitation, 12, 693

Kerr R. P., 1963, Physical Review Letters, 11, 237

Konoplya R. A., 2022, Physical Review D, 105, 044026

Kruskal M. D., 1960, Physical Review, 119, 1743

LIGO Scientific Collaboration, Virgo Collaboration, and KAGRA Collaboration 2021, Phys. Rev. D, 103, 122002

Maggio E., Pani P., Raposo G., 2022, Handbook of Gravitational Wave Astronomy, pp 1–37

Manikandan S. K., Rajeev K., 2022, Physical Review D, 105, 064024

Mathur S. D., 2005, Fortsch. Phys., 53, 793

Newman E. T., Couch E., Chinnapared K., Exton A., Prakash A., Torrence R., 1965, Journal of Mathematical Physics, 6, 918

Oshita N., Wang Q., Afshordi N., 2020, Journal of Cosmology and Astroparticle Physics, 2020, 016

Page D. N., 1993, Physical Review Letters, 71, 3743

Penrose R., 1965, Physical Review Letters, 14, 57

Raychaudhuri A. K., 1955, Physical Review, 98, 1123

Regge T., Wheeler J. A., 1957, Physical Review, 108, 1063

Schwarzschild K., 1916, Sitzungsberichte der Königlich Preussischen Akademie der Wissenschaften, pp 189–196

Singh T., Nandy M. K., 2024a, Phys. Scr., 99, 105008

Singh H., Nandy M. K., 2024b, Annals of Physics, 468, 169719

Szekeres G., 1960, Publicationes Mathematicae Debrecen, 7, 285

Wang Q., Oshita N., Afshordi N., 2020, Phys. Rev. D, 101, 024031